Where Is the Electronic Oscillator Strength? Mapping Oscillator Strength across Molecular Absorption Spectra

Lianjun Zheng[†], **Nicholas F. Polizzi**[‡], **Adarsh R. Dave**[§], **Agostino Migliore**[†,*], and **David N. Beratan**[†,‡,§,*]

[†]Department of Chemistry, Duke University, Durham, North Carolina 27708, United States

[‡]Department of Biochemistry, Duke University, Durham, North Carolina 27708, United States

[§]Department of Physics, Duke University, Durham, North Carolina 27708, United States

Abstract

The effectiveness of solar energy capture and conversion materials derives from their ability to absorb light and to transform the excitation energy into energy stored in free carriers or chemical bonds. The Thomas–Reiche–Kuhn (TRK) sum rule mandates that the integrated (electronic) oscillator strength of an absorber equals the total number of electrons in the structure. Typical molecular chromophores place only about 1% of their oscillator strength in the UV–vis window, so individual chromophores operate at about 1% of their theoretical limit. We explore the distribution of oscillator strength as a function of excitation energy to understand this circumstance. To this aim, we use familiar independent-electron model Hamiltonians as well as first-principles electronic structure methods. While model Hamiltonians capture the qualitative electronic spectra associated with π electron chromophores, these Hamiltonians mistakenly focus the oscillator strength in the fewest low-energy transitions. Advanced electronic structure methods, in contrast, spread the oscillator strength over a very wide excitation energy range, including transitions to Rydberg and continuum states, consistent with experiment. Our analysis rationalizes the low oscillator strength in the UV–vis spectral region in molecules, a step toward the goal of oscillator strength manipulation and focusing.

Graphical Abstract
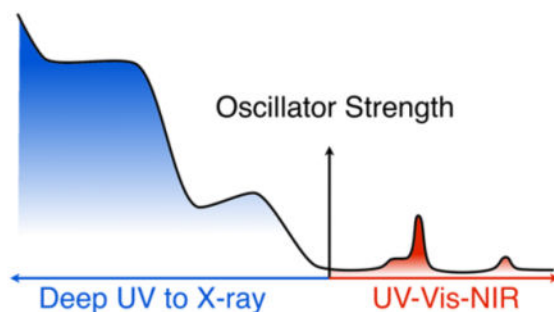
1. INTRODUCTION

Effective use of solar energy requires matching the electronic transitions of light-harvesting structures to the solar irradiance at the earth's surface.[1] Producing stronger absorbers would reduce the required thickness of light-absorbing materials, enhancing free charge carrier collection, optimizing voltage generation and fill factors, and lowering the cost of solar energy utilization.[2] Despite its obvious benefits to solar energy conversion, the development of better light absorbers in the UV–vis spectral region has been at most incremental. Ultrathin films of 10–20 nm can be used in specialized light-harvesting systems, assisted by plasmonic enhancement effects.[3–5] But how does electronic structure set fundamental limits on the characteristics of molecular light absorbers?

The Thomas–Reiche–Kuhn (TRK) sum rule[6] indicates that the integrated oscillator strength (OS) for a molecule is equal to its total number of electrons (N_e), i.e.

$$\sum_{k>0} f_{0k} = N_e \quad (1)$$

where the OS (f) is related to the molar absorption coefficient $\varepsilon(\nu)$ by

$$f_{0k} = \frac{2m_e}{3\hbar^2}(E_k - E_0)|\mathbf{r}_{0k}|^2 \quad (2a)$$

$$= \frac{4m_e c\varepsilon_0}{3N_A e^2}\int \varepsilon(\nu)\,\mathrm{d}\nu \quad (2b)$$

where m_e is the electron mass, and $e\mathbf{r}_{0k}$ is the transition dipole matrix element between the ground state $|\Psi_0\rangle$ and the kth excited state $|\Psi_k\rangle$:

$$\mathbf{r}_{0k} = \langle \Psi_0 | \hat{r} | \Psi_k \rangle \quad (3)$$

E_0 and E_k are the corresponding electronic energies.

In principle, the OS of a single transition could be as large as N_e. Since "strong" molecular OSs in the UV–vis spectral region are near unity,[7] and absorbers like porphyrins have over 160 electrons, the UV–vis OS may be at least 100-fold larger. Any rational strategy to "focus" this wasted OS on the UV–vis region must derive from a detailed understanding of the nature of the OS distribution in molecules. However, limited attention has been devoted, so far, to analyzing the OS distribution as a function of excitation energy in molecules. The aim of this paper is to learn how OS is distributed as a function of excitation energy in typical chromophores, using the TRK sum rule as a fundamental quantum mechanical constraint.

OS distributions are known for hydrogenic atoms and for some of the noble gases.[8–11] 44% of the OS for the H atom and 75% of the OS for the He atom are accounted for by transitions to continuum states.[6,9] In contrast, the continuum transitions of alkali atoms are weaker: the integrated OS values associated with transitions to the continuum for Li and Na are 2.4% and 0.21%, respectively.[9,11–13] These results indicate a wide range of possible behaviors at the atomic level, and point to a potential richness that may be accessed to manipulate OS distributions in molecules as a part of chromophore design. Studies of organic chromophores have been limited mainly to the UV–vis region, but lessons learned about the OS distributions of other atomic and molecular species may point toward strategies that could be transferred to organic chromophore design. K. Krishan et al.[14] studied some features of the continuum contribution to the total OS for a three-dimensional square well of finite width and depth. The continuum contribution was found to be about 30% for well depths that support just two bound states. The percentage of the OS associated with the transitions to the continuum dropped as the excited state became more strongly bound. Our aim is to explore the dependence of the OS distribution on model Hamiltonian parameters and on molecular structure.

The analysis described here maps how the OS in popular molecular absorbers is distributed over transitions to valence excited states, Rydberg states, and continuum states. We begin with time-dependent density functional theory (TDDFT) calculations of OS distributions for polyenes and porphyrins (section 2), and show that the UV–vis OS only captures a small fraction of the N_e value promised by the TRK sum rule. Simple independent-electron models and Hückel methods explored in section 3 predict that the OS associated with the low-energy transitions in polyenes and porphyrins could be as high as 80%. In order to explore where the OS is lost, section 4 analyzes the distribution of OS over excitation energies above the UV–vis window, using electronic structure theory as well as piecewise constant potential independent-electron models. In addition to full-electron calculations, we use TDDFT computations with frozen-core electrons to determine the OS associated with core, σ, and π electron excitations to bound and continuum states.

2. OS DISTRIBUTIONS FROM TDDFT

In order to understand OS distributions in real molecules and to link them to molecular electronic structures, we performed extensive DFT and TDDFT computations on polyenes and porphyrins. Polyenes were chosen because they enable a straightforward comparison

with the widely used infinitely deep 1D particle-in-a-box (1DPIB) model. Porphyrins are among the most studied systems for light-harvesting purposes.

We used the NWChem[15] computational chemistry package to calculate transition energies, OSs, and OS sums for polyenes (C_2H_4, C_4H_6, …, $C_{14}H_{16}$) and porphyrins (porphine and zinc-porphyrin). The B3LYP hybrid functional[16,17] was used. This density functional has given accurate excitation energy estimates for low-lying electronic excitations in ethylene and porphine.[18] TDDFT calculations of Rydberg state vertical excitation energies in organic molecules may suffer from large errors.[19] The calculation of valence states dominated by ionic character[20,21] and long-range charge-transfer transitions[22,23] may also be subject to relatively large errors. Such errors result from the poor asymptotic behavior of standard density functionals. In this study, we used the Casida–Salahub '00 asymptotic correction[19,24] to the B3LYP exchange-correlation potential to obtain its correct $-1/r$ long-distance behavior. This correction reduces the average error in computed excitation energies for ethylene and for porphine Q, B, N, and L bands, because of its balanced description of electronic transitions that involve valence and Rydberg states.[24] The cc-pVDZ, cc-pVTZ, aug-cc-pVTZ, and aug-cc-pVQZ basis sets were used for C_2H_4 and C_4H_6. The cc-pVDZ and cc-pVTZ basis sets were used for longer polyenes and for the porphyrins. It was shown that the OSs are not particularly sensitive to the basis set used: OSs of valence excitations are at convergence with the 6–31G basis set, and those of Rydberg transitions are at convergence with only one diffuse function added to the heavier atoms.[25,26] Despite the errors in the values of the single excitation energies (up to 1 eV for large π systems with small basis sets[20,26]), it is expected that the OS integrated over a relatively wide excitation energy range is not significantly affected by subtle changes in the excitation energies. Moveover, it was shown that the symmetries and ordering of the KS orbitals in small molecules are not influenced by the basis set size for basis sets such as 6–31G* or larger (note that the smallest basis set used here, i.e., cc-pVDZ, is of better quality than 6–31G* for describing electronic correlation).[27] A comparison of the accuracy of different methods for calculating OS distributions is provided in the Supporting Information. The electronic structure methods employed capture the main features of the OS distributions and provide an acceptable trade-off between accuracy and efficiency.

2.1. Polyenes

Figure 1a,b shows the integrated OS for ethylene as a function of the excitation energy obtained from TDDFT computations. The excitation energy-dependent integrated OS[29] is defined as the sum of the OSs associated with excitation energies below a given value E, i.e., $\Sigma_{(E_k - E_0) \leq E} f_{0k}$. This quantity is used to examine the convergence of the OS sum to N_e. The locally integrated OSs from our theoretical calculations (aug-cc-pVQZ basis set, Figure 1c) are in excellent agreement with the experiment-fitted results by A. Kumar et al.[28]

The C_2H_4 integrated OS (for excitation energies up to 40 eV) is equal to 10.5 in the TDDFT/cc-pVTZ calculations (Figure 1a). The total OS predicted by the TRK sum rule is 16. The remaining 34% of the OS is therefore assigned to higher energy transitions that may involve core electron or valence state transitions to higher-energy states. Figure 1b shows that the OS is spread widely over the 40 eV range sampled, where the strongest single OS is

0.94 at 29.5 eV. The lowest-energy transition in Figure 1b occurs at 7.54 eV, with an OS of 0.33. As with ethylene, the integrated OS for butadiene (Figure 2) increases approximately linearly and converges to $N_e = 30$ very slowly as a function of excitation energy. At 40 eV, the integrated OS is 17, i.e., 57% of the TRK total.

The butadiene OS is distributed over a wide range of excitation energies (Figure 2b). Nevertheless, the lowest-energy transition is characterized by the largest OS value (0.66). This is consistent with the theoretical results of Boechat-Roberty et al.[30]

Figure 3a summarizes the integrated OS distributions for $C_{2n}H_{2n+2}$ ($n = 1, 7$). The lowest-excitation energy drops, and its OS grows with chain length. Figure 3b highlights the linear growth of the OS associated with the ground-to-first excited state $S_0 \rightarrow S_1$ transition as a function of chain length. The fraction of OS in the $S_0 \rightarrow S_1$ transition increases with n. The OS of the polyenes is spread over a large excitation energy window, and the integrated OS converges very slowly to the TRK limit. The OS associated with the lowest-energy electronic transition is less than 20% of the number of π electrons ($N_{\pi e}$). We use $N_{\pi e}$ to facilitate comparison with the model Hamiltonians in section 3, where only π electrons are described by the models. This lowest-energy OS grows approximately linearly with molecular size, similar to that found in the 1DPIB model (see section 3.1).

2.2. Porphyrins

Porphyrins are widely used for energy harvesting[31] and charge separation.[32] Figure 4a shows the integrated OS of porphine and zinc porphyrin based on TDDFT analysis. McHugh et al.[33] calculated the OSs of porphine with the SCMO-PPP-CI (self-consistent molecular orbital-Pariser–Parr–Pople configuration interaction) method, finding excellent agreement with the measured spectra. Our results are in good agreement with McHugh's results. However, we explore a much wider excitation energy range with comparable accuracy, thus enabling the analysis of the OS distribution including transitions to the continuum.

No significant difference is found between the integrated OS curves of porphine and zinc porphyrin (Figure 4a). Table 1 indicates the characteristics of the four major peaks in the OS distribution. The four largest OS transitions capture ~13% of $N_{\pi e}$ ($N_{\pi e} = 18$ for porphine), even less than $\frac{f_{S_0 \rightarrow S_1}}{N_{\pi e}}$ found for polyenes (see Figure 3b). In porphyrins, the OS is spread over a dense set of electronic excited states, and spans a large range of values.

In summary, the OS captured by low-energy transitions in polyenes and porphyrins is far less than $N_{\pi e}$, and the integrated OS converges to the full TRK sum very slowly. In the simple harmonic oscillator model, however, 100% of the OS for excitations from the ground state is focused in the HOMO $\rightarrow$ LUMO transition (see section S1.1). Is the slow convergence to the TRK sum a robust feature of such molecular systems? To explore this question, we employ the tools of model Hamiltonian analysis in the following section.

3. OS IN MODEL POTENTIALS AND HÜCKEL MODELS

In this section, we study the OS distributions computed using empirical independent-electron Hamiltonians, including Hückel calculations. Comparing simple model and TDDFT

results, we identify specific OS spreading mechanisms (beyond the UV–vis frequency region) in molecules (section 4). This knowledge provides a starting point for future electronic structure-based OS focusing strategies.

3.1. Independent-Electron Models

Infinitely Deep Well (Particle-in-a-Box)—The 1DPIB model is often used to describe size quantization effects in molecules and nanoparticles.[34,35] In modeling linear conjugated molecules, we assume that the width of the well (W) grows in proportion to the number of electrons (Z). With an average C–C bond length of $R = 1.4$ Å, $Z = 4$, and $W = 4R$, we use the 1DPIB model to describe the π electrons of butadiene. Similar modeling is used for longer polyenes.

Figure 6a shows the integrated OS distributions for 1DPIB modeled polyenes with $Z = 2$–8 (C_2H_4–C_8H_{10}). The integrated OS converges to Z very rapidly for the 1DPIB model (Figure 6). The OS associated with the HOMO $\rightarrow$ LUMO transition ($f_{H\rightarrow L}$) depends linearly on the well width, but it represents a decreasing percentage of the total OS as the number of electrons grows (see inset in Figure 6b), while the opposite trend was found for the TDDFT calculations (Figure 3). The percentage plateaus to ~80% as $Z \rightarrow 50$ (see Figure S1.2). The 1DPIB model predicts considerably stronger OS focusing than is observed in π electron organic chromophores (~13%), and we explore the physical underpinnings of this behavior in section 4.

Constant Potential Particle-in-a-Ring—The constant (infinitely deep) particle-in-a-ring (PIR) potential is widely used to describe cyclic aromatic molecules. As in the case of the harmonic oscillator, OS is focused entirely in the HOMO $\rightarrow$ LUMO transitions for the PIR (see section S1.3). Subtleties associated with use of the TRK sum rule for this Hamiltonian were described by E. Hadjimichael et al.[36]

3.2. Hückel Model Calculations

The characteristics of the OS distributions described in section 3.1 are very different from those of real molecules. Does the strong OS focusing by the model Hamiltonians arise from the lack of atomistic "graininess" in the potential functions or from the absence of continuum states? We begin to address these questions by using the tight-binding π electron (i.e., Hückel) Hamiltonian.

Molecular orbitals $|\psi_n\rangle$ and their energy eigenvalues E_n were computed. 2p orbitals were described with a STO-3G basis. For polyenes, carbon atoms were separated by 1.4 Å along the molecular axis. The (gas-phase) atomic coordinates of porphine (see Figure 5a) were taken from DFT energy minimization calculations (B3LYP/cc-pVDZ). Hückel-level OSs were calculated using eqs 2a and 3 (see section S2 for details).

Polyenes—Figure 7a shows the integrated OS for polyenes as a function of excitation energy. In a comparison with the 1DPIB model (Figure 6a), the OS is somewhat less concentrated in the HOMO $\rightarrow$ LUMO transition, especially for longer chains. For example, 40% of the total OS is associated with the HOMO $\rightarrow$ LUMO transitions for $N_{\pi e} = 12$ (i.e.,

for $C_{12}H_{14}$; see inset in Figure 7b). The absolute OS values depend on the choice of Hamiltonian parameters (e.g., the nearest-neighbor couplings and the site energies, see section S2). The OS sum rule is not strictly obeyed for this system (see Figure 7 and Figure S2.1), as the Hückel Hamiltonian is not constructed to obey the commutation rules underpinning the sum rule. Nevertheless, the Hückel model provides us with valuable insights into OS distributions in real molecules.

The slower convergence of the integrated OS to the total OS in the Hückel model (compared to the constant potential models) is explained by the extent of localization of the atomic basis functions $\{|\varphi_i\rangle\}$. In Figure S2.1, we use the following approximation: $\langle \varphi_p | \mathbf{r} | \varphi_q \rangle = \delta_{pq}\mathbf{R}_q$, where $\mathbf{R}_q$ is the position of atom q. With this approximation, the integrated OS is similar to that found in the 1DPIB model (Figure 6). The STO-3G basis causes spreading of the OS over more transitions, which more closely resembles the behavior of real molecules.

Porphine—The OS associated with each porphine excitation (see blue vertical lines in Figure 8b) has contributions from several orbital transitions. The HOMO → LUMO transition (lowest energy transition in Figure 8b) contributes 70% of the total OS using the δ approximation above.

In summary, the OS computed using model piecewise constant potentials and Hückel models is highly focused. Where is the OS in real organic molecules? And why does the OS not appear in the low-energy transitions as suggested by the simple models?

4. WHERE IS THE OSCILLATOR STRENGTH?

4.1. Two OS Sinks: Excitations from σ and Core Electrons and Excitation to Rydberg and Continuum States

We found that the OS is spread over a much wider energy range in the TDDFT analysis than in the independent-electron models. To understand the nature of OS spreading as a function of excitation energy, we analyze the TDDFT results of section 2.1. Transitions are classified as occurring to bound, continuum, or "mixed" states (Figure 9).

Figure 9a indicates that the integrated OSs of transitions to bound states and to mixed-character excited states converge to 1.85 and 1.95 for butadiene, respectively, when the excitation energy reaches 40 eV (exploring a wider excitation energy range does not substantially affect our main conclusions). This only accounts for about 10% of the total OS. The remainder of the OS (~80%) involves transitions to the continuum states (Table 2).

The above TDDFT results (Figure 9) indicate that the integrated OS associated with transitions to bound states continues to increase with energy for excitation energies above the ionization energy. This further increase arises from transitions of inner-shell electrons (e.g., electrons from σ-bonding orbitals and core electrons). To study the influence of core and σ transitions on OS, we used frozen-core TDDFT calculation methods (see section 4.3).

Table 2 indicates that most of the OS values for ethylene and butadiene reside in transitions to the continuum. Indeed, none of the model Hamiltonians studied here include continuum-like states. K. Krishan et al.[14] have raised issues related to the use of free-particle states to

calculate the continuum contribution to the OS distribution for a three-dimensional square well: a pure plane wave does not properly describe the wave functions of low-lying continuum states near a potential well. Therefore, we next construct an embedded-well, piecewise-constant potential model to evaluate the influence of continuum-like transitions on the OS distributions (see section 4.2). Instead of using plane waves or the indirect evaluation of the total OS associated with transitions to the continuum states, we describe the continuum states explicitly, including the influence of the inner potential well on the continuum states.

4.2. Exploring Transitions to Continuum States with a Model Hamiltonian

Motivated by the TDDFT finding of a large amount of OS in transitions to the continuum, we built an embedded-well model (Figure 10). Continuum-like states arise from the wide outer region of the potential ($L \gg W$, see section S4 for parameters). This model allows us to assess the fraction of OS in valence-to-valence and valence-to-continuum transitions.

Width of the Continuum Region (L)—To evaluate the influence of L on the OS distribution, we set $W = 4R$ (with $R = 1.4$ Å) to simulate butadiene, and $\varepsilon = 10$ eV to produce a HOMO energy equal to the ionization potential (IP) of butadiene. L was varied from $40R$ to $200R$ (Figure 11).

The energy eigenvalues of the bound states ($E < 0$) vary weakly with L. In the "continuum" region ($E > 0$), the density of states grows with L. The five integrated OS curves in Figure 11b computed for different L values are nearly superimposable. Therefore, the influence of the continuum region width on the OS distribution is weak for L much larger than W. This model can also be used with smaller L/W ratios to examine the effects of quasicontinuum states on the OS distributions (e.g., the delocalized bound states that are responsible for the blue tail in the optical absorption spectrum of the solvated electron[39]).

Embedded-Well vs 1DPIB Model—For the embedded-well model, we choose $\varepsilon = 13$ eV so that the HOMO energies correspond to the IPs of typical polyenes. L is set to $100R$ to model the continuum. W was varied from $2R$ to $14R$ to mimic C_2H_4–$C_{14}H_{16}$ structures. The integrated OS distributions and the $f_{H\rightarrow L}$ values for $Z = 2$–8 are shown in Figure 12.

The OS becomes appreciable in the embedded-well model at excitation energies that are closer to those found in the TDDFT calculations (Figure 3) than to those found in the 1DPIB model (Figure 6). However, the integrated OS converges to Z quite rapidly in the embedded-well model, and the absolute values of $f_{H\rightarrow L}$ are close to Z. Thus, the presence of transitions to continuum states has little influence on the OS distributions found in the simpler 1DPIB model. This similarity probably arises because the depth of the internal well (ε) in the embedded-well model is large enough to cause its optical properties to mimic those of the infinitely deep well.

Binding Energy (ε) — LUMO Energy—ε was reduced from 13 to 5 eV to produce shallow-well bound states (Figure 13). This parameter choice generates greater similarity between the TDDFT results and the embedded-well results for polyenes. The OS in Figure 13a is much smaller at low energies compared to that in Figure 12a, and the OS sum

converges to Z in the energy range 0–10 eV. The reduced well depth yields smaller $f_{H \to L}$ values, especially when $2 \le Z \le 8$. For example, $f_{H \to L}$ ($Z = 4$, $\varepsilon = 13$ eV) = 3.89, while $f_{H \to L}$ ($Z = 4$, $\varepsilon = 5$ eV) = 1.76. The linear relationship between $f_{H \to L}$ and Z is maintained for the embedded-well model, as in the polyenes. The dependence of $\frac{f_{H \to L}}{Z}$ on Z is also different for $\varepsilon = 13$ eV and $\varepsilon = 5$ eV: the former (inset, Figure 12b) is similar to the 1DPIB model (inset, Figure 6b), while the latter (inset, Figure 13b) is similar to the TDDFT results for polyenes (inset, Figure 3b).

To explain why smaller ε values decrease the OS focusing in the low-energy transitions, the energy levels for the two different values of ε are shown in Figure 14. For $\varepsilon = 13$ eV, several unoccupied states reside deeply in the bound-state energy regime. In contrast, for $\varepsilon = 5$ eV, the LUMO is the only bound unoccupied state. The energy of the LUMO is very close to 0 eV, leading to a large fraction of the wave function spreading outside the internal potential well. Thus, the wave function overlap between the HOMO and LUMO in Figure 14b is smaller than that in Figure 14a. As Z increases, the HOMO shifts to higher energies (toward the continuum region), and a larger portion of the wave function expands outside the inner well, thus leading to a larger overlap with the wave function of the quasicontinuum LUMO. Thus, the inset of Figure 13b shows an increasing $\frac{f_{H \to L}}{Z}$ as a function of Z. This behavior explains the monotonic increase of $\frac{f_{S_0 \to S_1}}{N_{\pi e}}$ as a function of the number of polyene C atoms in the TDDFT analysis (inset, Figure 3b). The appearance of discrete excited states near the continuum may produce a relatively large continuum contribution to the total OS.

The results of the embedded-well model share many characteristics with the TDDFT results. However, the integrated OS still converges to Z much more rapidly than in the TDDFT analysis, despite adjusting the parameters to mimic the dimensions and energetics of the bound-state region. The difference in OS convergence properties likely arises from the fact that electrons other than π electrons (i.e., σ and core electrons) are omitted from the embedded-well model. Thus, the OSs associated with transitions to *the continuum states* for polyenes likely have a strong contribution from core-to-continuum transitions.

The results of section 4.1 also indicate that ~20% of the OS associated with high excitation energy transitions arises from core–electron transitions to *bound states*. Therefore, we conclude that this fraction of the OS is lost mainly to σ and core electron transitions to the bound and continuum states for the polyenes. This hypothesis is explored in greater detail below.

4.3. Frozen-Core TDDFT Analysis of Core, σ, and π Electron Transitions to Bound and Continuum States

We carried out frozen-core electron TDDFT calculations to further analyze the conclusions reached above (sections 4.1 and 4.2), namely, that transitions from states other than those of π symmetry contribute to OS spreading. These calculations were performed by selectively allowing excitations only from the occupied π orbitals, or from the occupied π and σ orbitals, in the TDDFT calculations via the NWChem program suite (keyword "*freeze*"[15]). Results are shown in Figure 15a. Since the excited states are combinations of π^* and σ^*

orbitals, as well as diffuse functions, we further filtered out contributions of the $\pi-\pi^*$ transitions and plotted them in Figure 15b.

Transitions from the core, σ, and π electrons contribute 5%, 69%, and 26%, respectively, of the total OS at a cutoff excitation energy of 40 eV (Figure 15a). These transitions are further categorized into transitions to bound, continuum, and "mixed" states and are summarized in Table 3. For simplicity, OS contributions from transitions to the "mixed" state are equally partitioned into the bound and continuum bins.

Figure 15a shows that about 70% of the total OS for transitions below the cutoff excitation energy of 40 eV is lost to σ electron transitions, most of which are associated with transitions to continuum states. The OSs associated with π and σ electrons are comparable to their electron numbers (i.e., $N_{\pi e} = 4$ and $N_{\sigma e} = 12$), so we conclude that the OS associated with excitation energies above 40 eV arises mostly from core–electron transitions.

The pink line in Figure 15b can be compared to the Hückel results in Figure 7a, in the sense that both calculations capture only the $\pi \rightarrow \pi^*$ transitions. The integrated OS calculated with these two methods is similar. The difference between the blue and pink lines in Figure 15b explains why the OS in molecules is not as focused as is found with the empirical model Hamiltonians: 55% of the OS resides in transitions to high-lying σ^* orbitals and to diffuse functions, even when considering excitations only from π states.

5. CONCLUSIONS

Strongly absorbing organic and organometallic chromophores typically place 1% of their available OS in the UV–vis window. Our analysis finds that most of the OS is associated with transitions to Rydberg and continuum states. Interestingly, the sharing of OS with transitions to the continuum is familiar in the atomic physics of the hydrogen atom.[6] This feature of molecular OS distributions is not captured by simple independent-electron and empirical potential models, which focus the OS in the lowest-energy transitions to bound states. The transitions to Rydberg and continuum states in the OS are captured by the TDDFT analysis presented here. Indeed, the TDDFT analysis indicates that only ~13% of the porphyrin π electron OS is focused in the transition to the lowest-energy excited state, the so-called Q-band. The Hückel and particle-in-a-ring Hamiltonians predict convergence of the integrated OS to the TRK value (as a function of excitation energy) that is much faster than is predicted by the TDDFT analysis, and thus the independent-electron models overestimate the OS of the lowest-energy transitions.

For polyenes, the TDDFT OSs are distributed over a wide range of excitation energies beyond the UV–vis window, and the integrated OS converges slowly to the electron number. We find that the OS of the lowest-energy transition captures a small fraction of the total OS (<3%), but this percentage increases linearly with the number of carbon atoms.

Comparison of the results from TDDFT and model Hamiltonians allows us to understand and to describe quantitatively how OS is lost to excitations of core electrons or to continuum states. Our conclusions are summarized in Figure 16. A large portion (~70%) of the total OS is associated with the excitation of σ electrons, mostly to the continuum states. The

remaining 26% of the OS is associated with π electron transitions, and about 55% of this OS corresponds to transitions to σ^* orbitals and diffuse functions embedded in the continuum.

Understanding how molecular structure determines the OS distribution as a function of energy is a step toward developing purposeful strategies to redistribute and focus OS into specific excitation energy windows. Strategies that aim to increase OS in the UV–vis spectral region have involved plasmonic[3,40–42] and cavity enhancement effects.[43–46] We find here that any electronic structure-based strategy for focusing OS into the UV–vis region must effectively shut down core-to-bound and σ-to-continuum transitions. To perturb molecular electronic structure, such strategies might employ tailored electromagnetic fields,[47] structural redesign of chromophores and chromophore assemblies, and tailored molecule–nanostructure assemblies. [48,49] Even a modest focusing of the UV–vis OS, achieved via design, could dramatically increase the efficiency of current photovoltaic devices.

Supplementary Material

Refer to Web version on PubMed Central for supplementary material.

Acknowledgments

References

1. Bird RE, Hulstrom RL, Lewis L. Terrestrial Solar Spectral Data Sets. Sol Energy. 1983; 30:563–573.

2. Schiff, EA.; Hegedus, S.; Deng, X. Handbook of Photovoltaic Science and Engineering. Luque, A.; Hegedus, S., editors. John Wiley & Sons; New York: 2011. p. 487-545.

3. Hägglund C, Zeltzer G, Ruiz R, Thomann I, Lee HBR, Brongersma ML, Bent SF. Self-Assembly Based Plasmonic Arrays Tuned by Atomic Layer Deposition for Extreme Visible Light Absorption. Nano Lett. 2013; 13:3352–3357. [PubMed: 23805835]

4. Yan W, Tao Z, Ong TMB, Gu M. Highly Efficient Ultrathin-Film Amorphous Silicon Solar Cells on Top of Imprinted Periodic Nanodot Arrays. Appl Phys Lett. 2015; 106:093902.

5. Gusak V, Kasemo B, Hägglund C. High Aspect Ratio Plasmonic Nanocones for Enhanced Light Absorption in Ultrathin Amorphous Silicon Films. J Phys Chem C. 2014; 118:22840–22846.

6. Bethe, HA.; Salpeter, EE. Quantum Mechanics of One-and Two-Electron Atoms. Academic Press; New York: 1957. p. 255-262.

7. Turro, NJ. Modern Molecular Photochemistry. University Science Books; Sausalito, CA: 1991.

8. Watson W. Photoionization of Helium, Neon and Argon in the 60–230 eV Photon Energy Range. J Phys B: At Mol Phys. 1972; 5:2292–2303.

9. Wheeler JA. Theory of the Dispersion and Absorption of Helium. Phys Rev. 1933; 43:258–263.

10. Ditchburn RW, Jutsum PJ, Marr GV. The Continuous Absorption of Light in Alkali-Metal Vapours. Proc R Soc London, Ser A. 1953; 219:89–101.

11. Fano U, Cooper J. Spectral Distribution of Atomic Oscillator Strengths. Rev Mod Phys. 1968; 40:441–507.

12. Trumpy B. Transition probabilities in the Lithium Atom. Eur Phys J A. 1929; 54:372–384.

13. Trumpy B. Continuous Absorption in Lithium and Sodium. Eur Phys J A. 1931; 71:720–734.

14. Krishan K, Banerjee K. Continuum Contributions to Polarizability, Absorption Coeffcient and Total Oscillator Strength. Chem Phys Lett. 1969; 3:679–683.

15. Valiev M, Bylaska EJ, Govind N, Kowalski K, Straatsma TP, Van Dam HJ, Wang D, Nieplocha J, Apra E, Windus TL. NWChem: A Comprehensive and Scalable Open-Source Solution for Large Scale Molecular Simulations. Comput Phys Commun. 2010; 181:1477–1489.

16. Lee C, Yang W, Parr RG. Development of the Colle-Salvetti Correlation-Energy Formula into a Functional of the Electron Density. Phys Rev B: Condens Matter Mater Phys. 1988; 37:785–789.

17. Becke AD III. Density-Functional Thermochemistry. III. The Role of Exact Exchange. J Chem Phys. 1993; 98:5648–5652.

18. Bauernschmitt R, Ahlrichs R. Treatment of Electronic Excitations within the Adiabatic Approximation of Time Dependent Density Functional Theory. Chem Phys Lett. 1996; 256:454–464.

19. Casida ME, Jamorski C, Casida KC, Salahub DR. Molecular Excitation Energies to High-Lying Bound States from Time-Dependent Density-Functional Response Theory: Characterization and Correction Of the Time-Dependent Local Density Approximation Ionization Threshold. J Chem Phys. 1998; 108:4439–4449.

20. Parac M, Grimme S. A TDDFT Study of the Lowest Excitation Energies of Polycyclic Aromatic Hydrocarbons. Chem Phys. 2003; 292:11–21.

21. Grimme S, Parac M. Substantial Errors from Time-Dependent Density Functional Theory for the Calculation of Excited States of Large π Systems. ChemPhysChem. 2003; 4:292–295. [PubMed: 12674603]

22. Paddon-Row MN, Shephard MJ. A Time-Dependent Density Functional Study of the Singlet-Triplet Energy Gap in Charge-Separated States of Rigid Bichromophoric Molecules. J Phys Chem A. 2002; 106:2935–2944.

23. Dreuw A, Weisman JL, Head-Gordon M. Long-Range Charge-Transfer Excited States in Time-Dependent Density Functional Theory Require Non-Local Exchange. J Chem Phys. 2003; 119:2943–2946.

24. Hirata S, Zhan CG, Aprá E, Windus TL, Dixon DA. A New, Self-Contained Asymptotic Correction Scheme to Exchange-Correlation Potentials for Time-Dependent Density Functional Theory. J Phys Chem A. 2003; 107:10154–10158.

25. Matsuzawa NN, Ishitani A, Dixon DA, Uda T. Time-Dependent Density Functional Theory Calculations of Photo-absorption Spectra in the Vacuum Ultraviolet Region. J Phys Chem A. 2001; 105:4953–4962.

26. Ciofini I, Adamo C. Accurate Evaluation of Valence and Low-Lying Rydberg States with Standard Time-Dependent Density Functional Theory. J Phys Chem A. 2007; 111:5549–5556. [PubMed: 17542570]

27. Stowasser R, Hoffmann R. What Do the Kohn-Sham Orbitals and Eigenvalues Mean? J Am Chem Soc. 1999; 121:3414–3420.

28. Kumar A, Jhanwar B, Meath W. Dipole Oscillator Strength Distributions, Properties, and Dispersion Energies for Ethylene, Propene, and 1-Butene. Can J Chem. 2007; 85:724–737.

29. Kumar A, Meath WJ. Dipole Oscillator Strength Properties and Dispersion Energies for Acetylene and Benzene. Mol Phys. 1992; 75:311–324.

30. Boechat-Roberty HM, Uhl EO, Rodrigues FN, Lopes MCA, Rocco MLM, Lucas CA, Rocha AB, Bielschowsky CE, de Souza GGB. Electron Scattering from Trans 1, 3-Butadiene Molecule: Cross-Sections, Oscillator Strength and VUV Photo-absorption Cross-Sections. Eur Phys J D. 2013; 67:26–31.

31. Li LL, Diau EWG. Porphyrin-Sensitized Solar Cells. Chem Soc Rev. 2013; 42:291–304. [PubMed: 23023240]

32. Amdursky N, Ferber D, Pecht I, Sheves M, Cahen D. Redox Activity Distinguishes Solid-State Electron Transport from Solution-Based Electron Transfer in a Natural and Artificial Protein: Cytochrome C and Hemin-Doped Human Serum Albumin. Phys Chem Chem Phys. 2013; 15:17142–17149. [PubMed: 24008341]

Author Manuscript

Author Manuscript

Author Manuscript

Author Manuscript

33. McHugh A, Gouterman M, Weiss C Jr. Porphyrins XXIV. Energy, Oscillator Strength, and Zeeman Splitting Calculations (SCMO-CI) for Phthalocyanine, Porphyrins, and Related Ring Systems. Theor Chim Acta. 1972; 24:346–370.

34. Kuhn H. Free Electron Model for Absorption Spectra of Organic Dyes. J Chem Phys. 1948; 16:840–841.

35. Steigerwald ML, Brus LE. Semiconductor Crystallites: A Class of Large Molecules. Acc Chem Res. 1990; 23:183–188.

36. Hadjimichael E, Currie W, Fallieros S. The Thomas-Reiche-Kuhn Sum Rule and the Rigid Rotator. Am J Phys. 1997; 65:335–341.

37. Casida, ME. Recent Advances in Density Functional Methods. World Scientific; River Edge, NJ: 1995. p. 155-192.

38. Casida M, Huix-Rotllant M. Progress in Time-Dependent Density-Functional Theory. Annu Rev Phys Chem. 2012; 63:287–323. [PubMed: 22242728]

39. Jacobson LD, Herbert JM. Polarization-Bound Quasi-Continuum States are Responsible for the "Blue Tail" in the Optical Absorption Spectrum of the Aqueous Electron. J Am Chem Soc. 2010; 132:10000–10002. [PubMed: 20608656]

40. Hägglund C, Apell SP, Kasemo B. Maximized Optical Absorption in Ultrathin Films and its Application to Plasmon-Based Two-Dimensional Photovoltaics. Nano Lett. 2010; 10:3135–3141. [PubMed: 20698628]

41. Wang KX, Yu Z, Liu V, Brongersma ML, Jaramillo TF, Fan S. Nearly Total Solar Absorption in Ultrathin Nanostructured Iron Oxide for Efficient Photoelectrochemical Water Splitting. ACS Photonics. 2014; 1:235–240.

42. Gu Q. Plasmonic Metallic Nanostructures for Efficient Absorption Enhancement in Ultrathin CdTe-Based Photovoltaic Cells. J Phys D: Appl Phys. 2010; 43:465101.

43. Kats MA, Blanchard R, Genevet P, Capasso F. Nanometre Optical Coatings Based on Strong Interference Effects in Highly Absorbing Media. Nat Mater. 2013; 12:20–24. [PubMed: 23064496]

44. Mann SA, Garnett EC. Extreme Light Absorption in Thin Semiconductor Films Wrapped around Metal Nanowires. Nano Lett. 2013; 13:3173–3178. [PubMed: 23758555]

45. Kats MA, Sharma D, Lin J, Genevet P, Blanchard R, Yang Z, Qazilbash MM, Basov D, Ramanathan S, Capasso F. Ultra-Thin Perfect Absorber Employing a Tunable Phase Change Material. Appl Phys Lett. 2012; 101:221101.

46. Song H, Guo L, Liu Z, Liu K, Zeng X, Ji D, Zhang N, Hu H, Jiang S, Gan Q. Nanocavity Enhancement for Ultra-Thin Film Optical Absorber. Adv Mater. 2014; 26:2737–2743. [PubMed: 24616090]

47. Cappel UB, Feldt SM, Schöneboom J, Hagfeldt A, Boschloo G. The influence of Local Electric Fields on Photoinduced Absorption in Dye-Sensitized Solar Cells. J Am Chem Soc. 2010; 132:9096–9101. [PubMed: 20552960]

48. Aydin K, Ferry VE, Briggs RM, Atwater HA. Broadband Polarization-Independent Resonant Light Absorption Using Ultrathin Plasmonic Super Absorbers. Nat Commun. 2011; 2:517. [PubMed: 22044996]

49. Würthner F, Kaiser TE, Saha-Möller CR. J-Aggregates: From Serendipitous Discovery to Supramolecular Engineering of Functional Dye Materials. Angew Chem, Int Ed. 2011; 50:3376–3410.

Author Manuscript
Author Manuscript
Author Manuscript
Author Manuscript
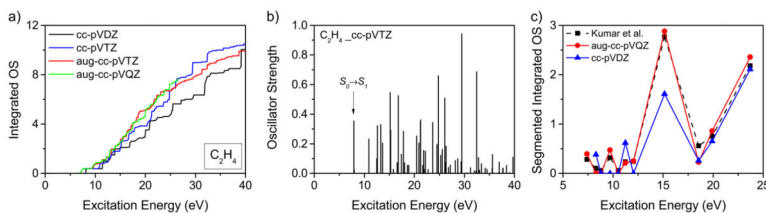
Figure 1.
Integrated OS and OS distribution of ethylene (C_2H_4) from TDDFT computation. (a) Integrated OS as a function of excitation energy calculated with the indicated basis sets. (b) OS distribution using the cc-pVTZ basis set. (c) Comparison of our results calculated by means of the aug-cc-pVQZ and cc-pVDZ basis sets (solid lines) with empirical results from A. Kumar et al.[28] (dashed line). For each data point: the *x*-coordinate is the average energy of each excitation energy interval; the *y*-coordinate is the OS integrated in the corresponding energy windows. Note that the UV–vis energy region is 1.6–12.4 eV, but solar radiation of energy higher than 4.5 eV is completely absorbed by the atmosphere.
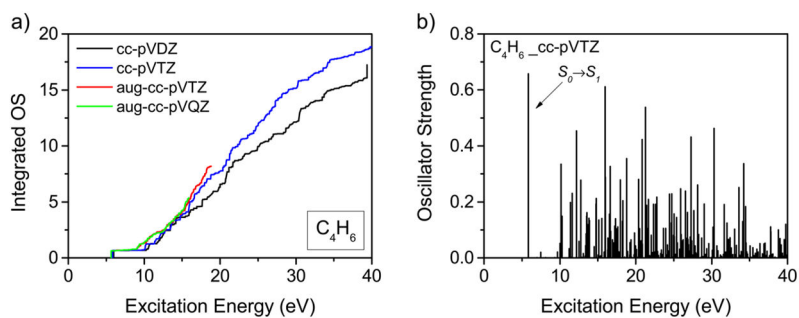
Figure 2.
OS distribution of *trans*-butadiene (C_4H_6) from TDDFT computations: (a) integrated OSs as a function of excitation energy calculated with varied basis sets; (b) OS distribution calculated with the cc-pVTZ basis set. Similarly to ethylene, the integrated OS converges to the TRK sum very slowly.
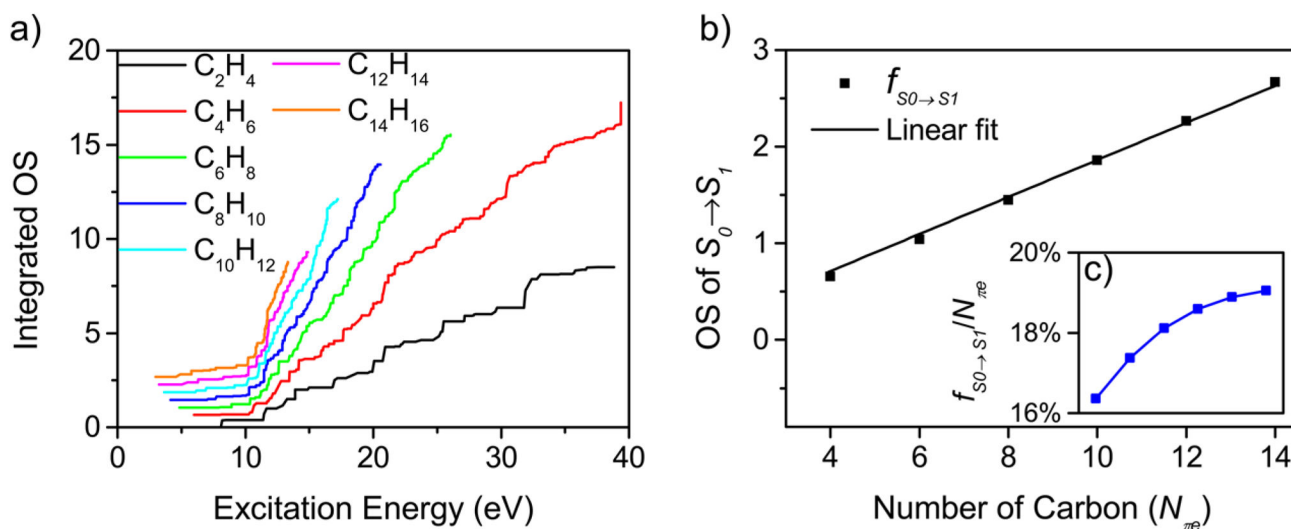
Figure 3.
(a) Integrated OS for polyenes based on TDDFT computations using the cc-pVDZ basis set.
(b) The OS associated with the lowest-energy transition ($f_{S_0 \to S_1}$) for each molecule and a

linear fit of $f_{S_0 \to S_1}$ vs $N_{\pi e}$. The inset shows $\frac{f_{S_0 \to S_1}}{N_{\pi e}}$ vs $N_{\pi e}$ for each molecule. The scale of the x-axis is the same as in part b. Note that the OSs for all polyenes are distributed over a large range of excitation energies. The $f_{S_0 \to S_1}$ captures 20% of $N_{\pi e}$ (which is much less than that predicted by simple model Hamiltonians; see section 3.1).
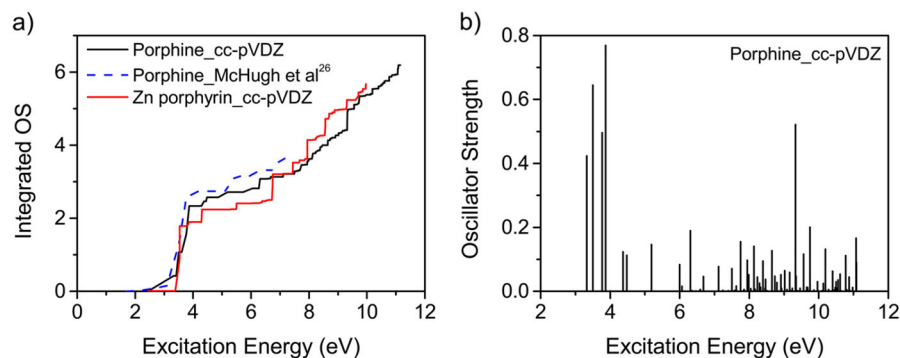
Figure 4.
Computed OS for porphyrins from TDDFT calculations with the cc-pVDZ basis set: (a) the integrated OSs of porphine (black solid line) compared with zinc-porphyrin (red solid line) and values from the literature (blue dashed line[33]); (b) OS vs excitation energy for porphine. The values indicated with the blue dashed lines are double the original computational results of McHugh et al., which refer to one transition of a degenerate electron pair. The OSs associated with transitions between frontier orbitals are much larger than other transitions shown in part b. However, these OSs only represent 13% of $N_{\pi e}$, which is even smaller than the fraction in polyenes.
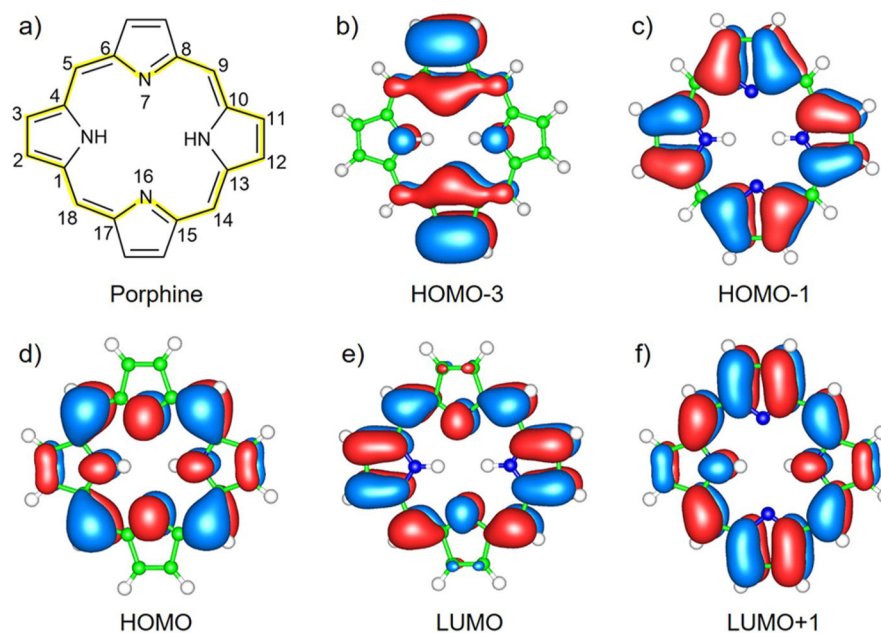
Figure 5.
(a) Chemical structure of porphine. The ring highlighted in yellow defines the conjugated network modeled in the Hückel calculations (see section 3.2). (b–f) Molecular orbitals of porphine involved in strong electronic transitions as determined using TDDFT. Small energy differences exist between the HOMO and HOMO − 1, as well as between the LUMO and LUMO + 1.
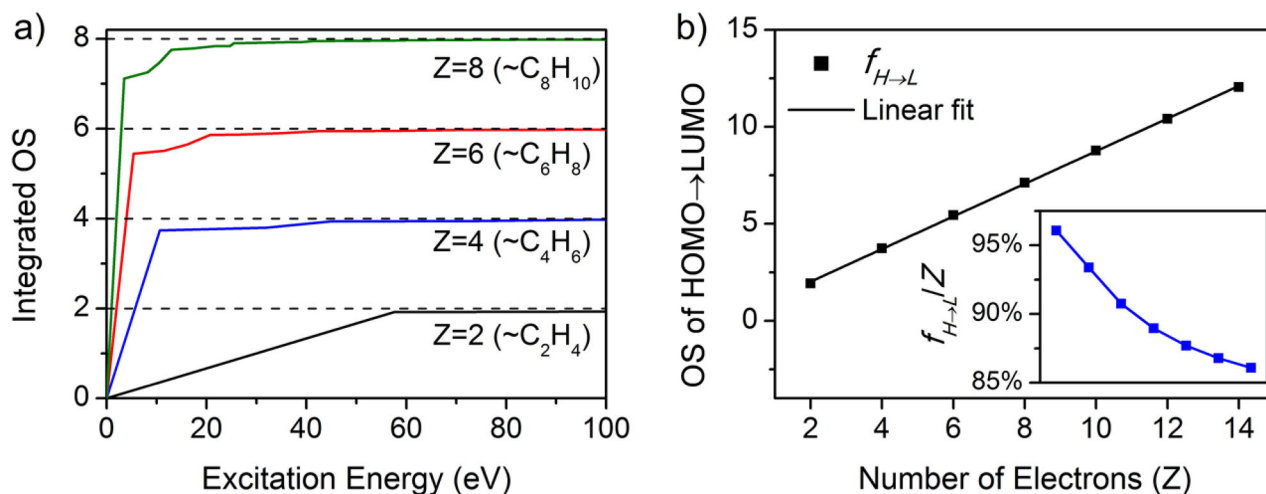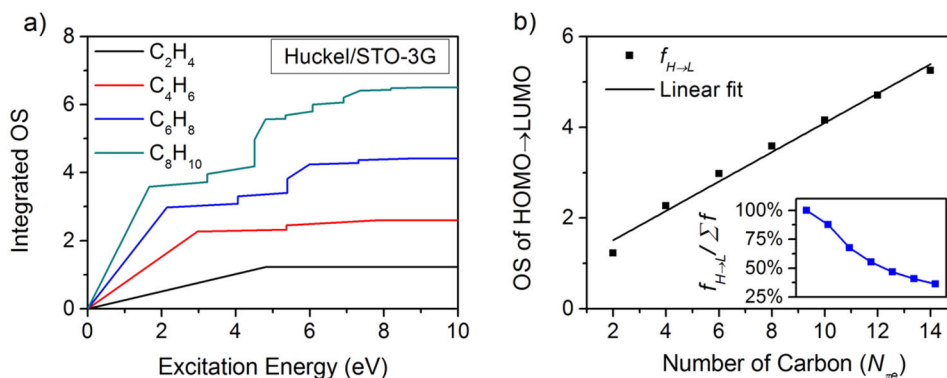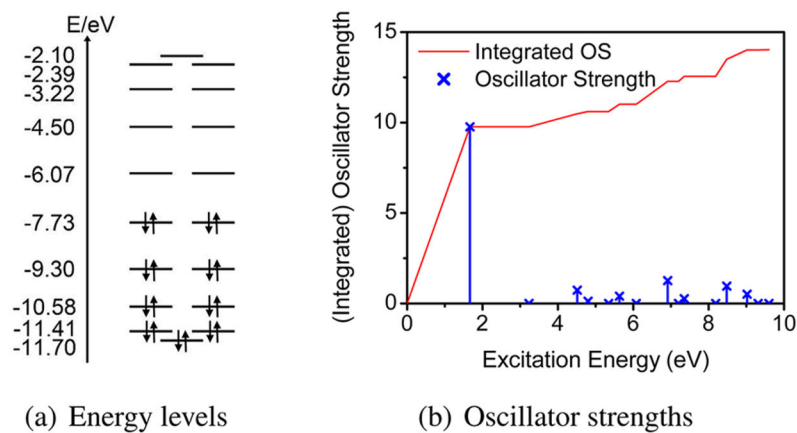
Figure 6.
Results from the 1DPIB calculations. (a) The integrated OS as a function of the excitation energy for $Z = 2, 4, 6, 8$ in the infinitely deep well models for the C_2H_4 to C_8H_{10} molecules. The horizontal dashed lines indicate the asymptotic value of the integrated OS according to the TRK sum rule. (b) The OSs of the HOMO → LUMO transitions ($f_{H \to L}$) for $Z = 2, 4, \ldots,$ 14 and a linear fitting of $f_{H \to L}$ vs Z. The inset shows the fraction of $f_{H \to L}$ over the total OS ($\frac{f_{H \to L}}{Z}$) vs Z. The range of the x-axis is the same as in part b. Note that the OS is sharply focused in the first few transitions, especially the HOMO → LUMO transition.
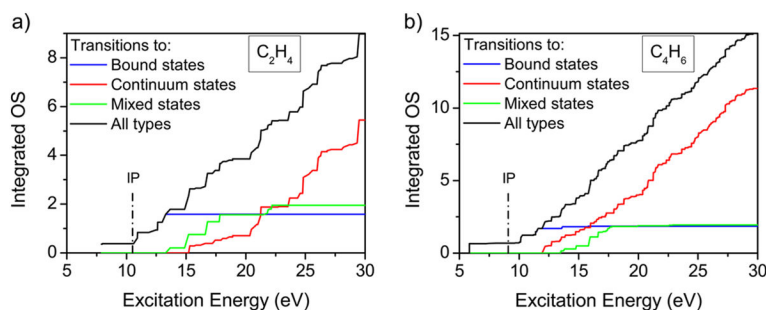
Figure 7.
Hückel analysis using one STO-3G p orbital per C atom, without neglect of atomic orbital overlap. (a) Integrated OS distributions of polyenes. (b) OSs of the HOMO → LUMO transition ($f_{H \to L}$) for the series of molecules and their linear fitting vs $N_{\pi e}$. The inset shows the fraction of $f_{H \to L}$ over the total OS ($\frac{f_{H \to L}}{\sum f}$; here, $\sum f$ does not converge to $N_{\pi e}$) vs $N_{\pi e}$ for each molecule. The scale of the x-axis is the same as in part b. Note that the OS is less focused compared to the analytical models described in section 3.1. $\frac{f_{H \to L}}{\sum f}$ drops from nearly 100% to an asymptote of ~30% as the length of the polyene grows.

(a) Energy levels (b) Oscillator strengths

Figure 8.
(a) Energy levels and (b) OS distribution (blue lines) and integrated OSs (red line) of porphine in the 0–10 eV energy range calculated by the Hückel method. The HOMO → LUMO transition (first blue line) contains 70% of the total OS for the π electron transitions included in this model.

Figure 9.
Integrated OS distributions of (a) ethylene and (b) butadiene from our TDDFT calculations using the cc-pVTZ basis set. Results are classified by the types of electronic transitions. TDDFT is a full-electron approach, where the ground and excited states wave functions can be written as an expansion of singly excited configurations.[37,38] The expansion coefficients can be assigned an "excitation character". In the figure, "bound states" denote excitations that are mostly (>90%) composed of transitions to bound states ($E < 0$). "Continuum states" denote excitations that are mostly (>90%) composed of transitions to continuum states ($E > 0$). "Mixed states" refer to excitations that consist of component transitions to both bound and continuum states, with each portion being at least 10%. OSs are integrated over each of these excitation types as a function of the maximum excitation energy. The dot-dashed line indicates the ionization potential (IP) of ethylene and butadiene.
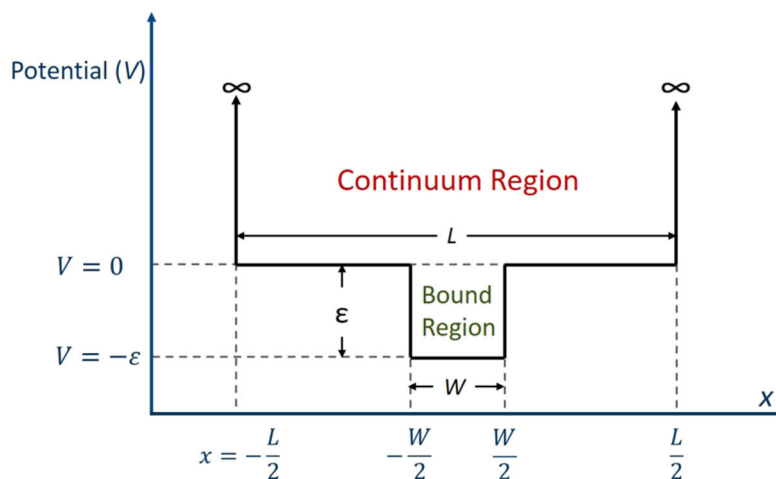
Figure 10.

Scheme for the embedded-well piecewise potential model. The potential in the region

$x \in \left(-\dfrac{W}{2}, \dfrac{W}{2} \right)$ is $V = -\varepsilon$, and the potential in the region $x \in \left(\pm\dfrac{L}{2}, \pm\dfrac{W}{2} \right)$ is $V = 0$. States with energy $E < 0$ are bound states, and states with energy E 0 model continuum states (this approximation is allowed by parameter choices such that $L \gg W$). ε is the depth of the internal well and determines the electron binding energy. W models the width of the molecular region. W is a dimensionless length in units of R, where $R = 1.4$ Å is a typical C–C bond length.

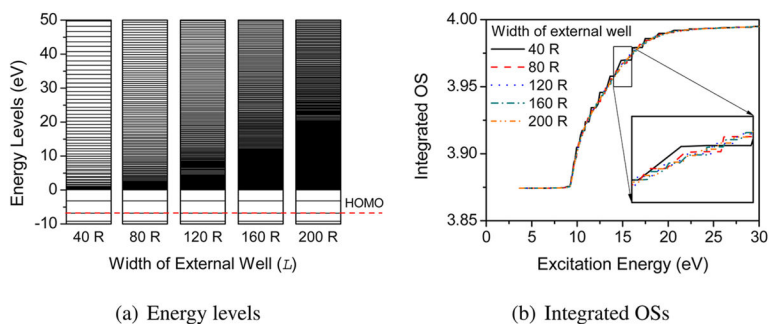(a) Energy levels

(b) Integrated OSs

Figure 11.
Results from the embedded-well model calculation with $\varepsilon = 10$ eV and $W = 4R$: (a) energy levels and (b) integrated OS distributions for $L = 40R$, $80R$, …, $200R$. The similarities of energy levels and integrated OS distributions for different L values indicate that the influence of the width of the external well is negligible for $L/W > 10$.
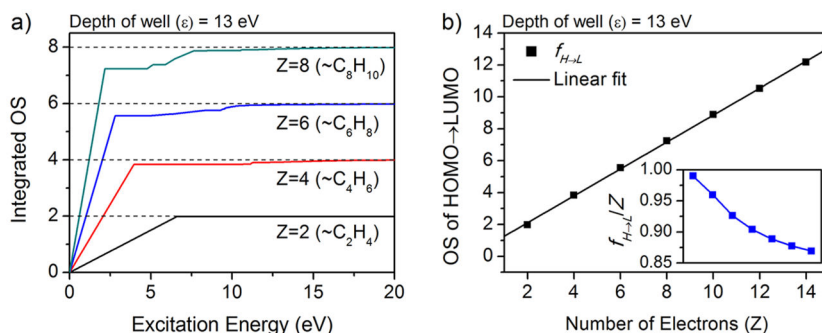
Figure 12.
Results of the embedded-well model calculation with $\varepsilon = 13$ eV, $L = 100R$. (a) Integrated OS as a function of the maximum excitation energy for $Z = 2$–8, which corresponds to C_2H_4–C_8H_{10}. The horizontal dashed lines are the asymptotic values of the integrated OSs for the different molecules based on the TRK sum rule. (b) OS of the HOMO → LUMO transition ($f_{H \rightarrow L}$) for $Z = 2, 4, \ldots, 14$ with a linear fitting of $f_{H \rightarrow L}$ vs Z. The inset shows $\frac{f_{H \rightarrow L}}{Z}$ vs Z for $Z = 2, 4, \ldots, 14$. Note that the OS distributions here are different from those of the TDDFT analysis. With the choice of internal well depth, the inclusion of the continuum states causes little change compared to the basic characteristics of the OS distributions from the 1DPIB model.
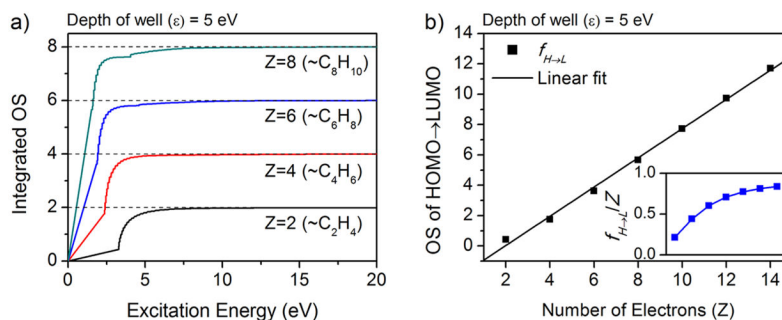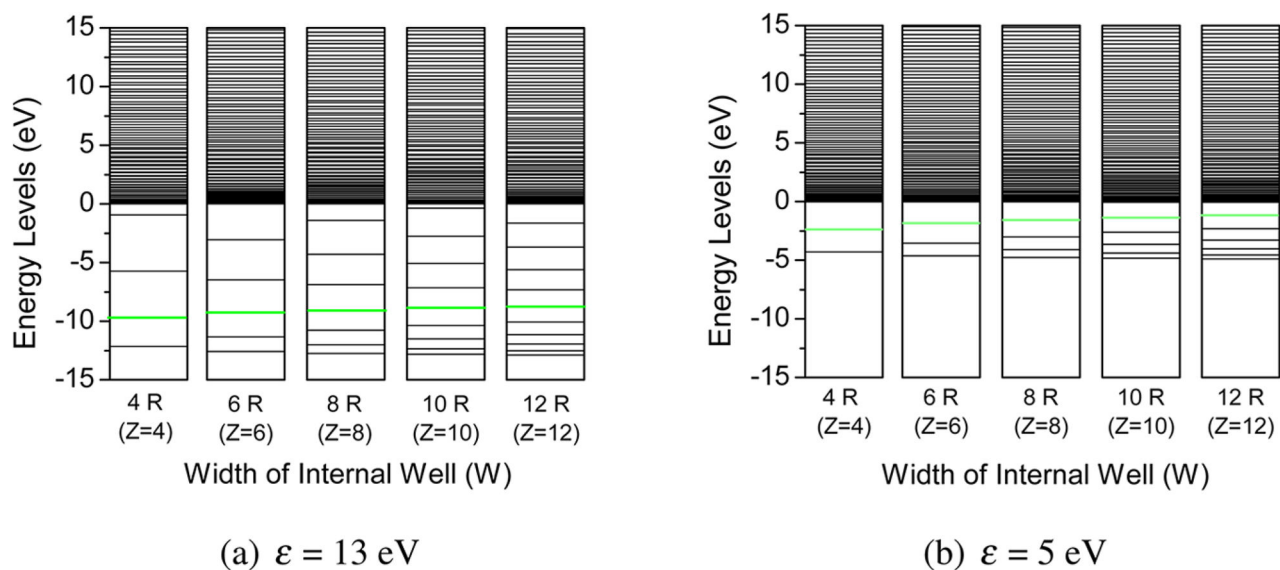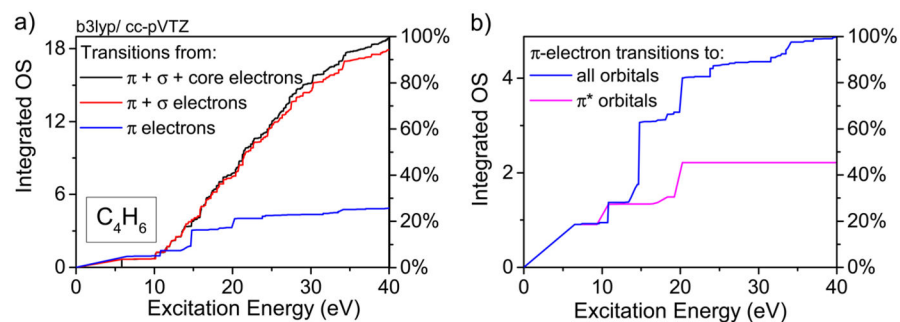
Figure 13.

Results from the embedded-well model calculation with $\varepsilon = 5$ eV and $L = 100R$. The value of ε was chosen to be much smaller than that in Figure 12 to avoid an infinitely deep well limit. In this case, the LUMO is located slightly below 0 eV, and it is thus more delocalized than the deeply bound LUMO for $\varepsilon = 13$ eV. (a) Integrated OS as a function of the maximum excitation energy for $Z = 2$–8, which corresponds to C_2H_4–C_8H_{10}. The horizontal dashed lines are the asymptotic values of the integrated OSs for the different molecules based on the TRK sum rule. (b) OS of the HOMO $\rightarrow$ LUMO transitions ($f_{H\rightarrow L}$) for $Z = 2, 4, \ldots, 14$ with a linear fitting of $f_{H\rightarrow L}$ vs Z. The inset shows the fraction of $f_{H\rightarrow L}$ over the total OS ($\frac{f_{H\rightarrow L}}{Z}$) vs Z for $Z = 2, 4, \ldots, 14$. Note that the OS converges to the TRK sum much more slowly than those found with $\varepsilon = 13$ eV. The inset curve is concave rather than convex (Figure 12), which is similar to the polyene results calculated using TDDFT. However, the integrated OS still converges to Z much faster than in molecules.

(a) $\varepsilon = 13$ eV

(b) $\varepsilon = 5$ eV

Figure 14.
Energy levels for $Z = 4, 6, 8, 10, 12$ (i.e., $W = 4R - 12R$) and a well depth of (a) 13 eV and (b) 5 eV, using the embedded-well model. The green line shows the HOMO of each system. Note that in part b the LUMOs lie in the bound region slightly below 0 eV, which may lead to a relatively large fraction of the wave function spreading outside the internal well. This explains why smaller ε values lead to decreased OS focusing in the HOMO $\rightarrow$ LUMO transition.

Figure 15.
Results from the TDDFT frozen-core calculations of C_4H_6 using the cc-pVTZ basis set. (a) Integrated OS distributions associated with transitions of the π electrons (blue), π and σ electrons (red), and all electrons (black). (b) Integrated OS distributions for excitations of the π electrons to all unoccupied orbitals (blue) and to the π^* orbitals (pink).
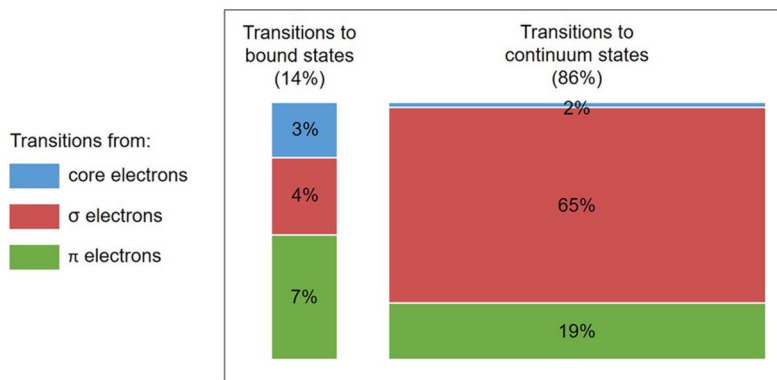
Figure 16.
OS distributions for different types of transitions in butadiene at the cutoff excitation energy of 40 eV from the analysis of TDDFT calculation results in section 4. About 70% of the total OS is lost to transitions from σ electrons, most of which is to the continuum states. Among all transitions, the continuum contribution is 86%.

Table 1

Major Components of the First Four Largest Contributors to the OSs of Porphine from TDDFT Calculations[a]

E (eV)	oscillator strength	major transitions					
		from	to	from	to	from	to
3.3285	0.42400	HOMO − 3	LUMO + 1	HOMO − 1	LUMO		
3.5056	0.64469	HOMO − 1	LUMO + 1	HOMO	LUMO	HOMO − 3	LUMO
3.7699	0.49596	HOMO − 3	LUMO				
3.8701	0.76937	HOMO − 3	LUMO + 1	HOMO − 1	LUMO		

[a]OSs are focused mostly in five transitions: HOMO − 3 → LUMO/LUMO + 1, HOMO − 1 → LUMO/LUMO + 1, HOMO → LUMO. The related orbitals are depicted in Figure 5b–f.

Table 2

Integrated OS for Each Type of Transition Defined in Figure 9 and Its Fraction over Σf for Ethylene and Butadiene

	bound states	mixed states	continuum states
C_2H_4	1.59 (15.1%)	1.95 (18.6%)	6.95 (66.3%)
C_4H_6	1.85 (9.8%)	1.95 (10.3%)	15.0 (79.9%)

Table 3

Integrated OS for Each Type of Transition from Core, σ, and π Electrons and Its Fraction over the Total OS for Butadiene

	bound states	continuum states	total
core electrons	0.6 (3%)	0.3 (2%)	0.9 (5%)
σ electrons	0.8 (4%)	12.2 (65%)	13.0 (69%)
π electrons	1.4 (7%)	3.5 (19%)	4.9 (26%)
total	2.8 (14%)	16.0 (86%)	18.9 (100%)